SciPost Phys. 21, 033 (2026)

Nonperturbative effects in triple-differential dijet and Z+jet production at the LHC

Stefan Gieseke[3⋆], Maximilian Horzela[1], Manjit Kaur[4], Dari Leonardi[3], Klaus Rabbertz[2†], Aayushi Singla[4] and Cedric Verstege[2]

1 II. Institute of Physics, Georg-August-Universität Göttingen, Friedrich-Hund-Platz 1, 37077 Göttingen, Germany
2 Institute of Experimental Particle Physics, Karlsruhe Institute of Technology, Wolfgang-Gaede-Str. 1, 76131 Karlsruhe, Germany
3 Institute for Theoretical Physics, Karlsruhe Institute of Technology, Wolfgang-Gaede-Str. 1, 76131 Karlsruhe, Germany
4 Department of Physics, Panjab University, Sector-14, 160014 Chandigarh, India

⋆ stefan.gieseke@kit.edu , † klaus.rabbertz@kit.edu

Abstract

In comparisons of precision measurements at colliders to the most accurate predictions available in perturbative quantum chromodynamics (QCD), it is required to correct for nonperturbative effects. By means of Monte Carlo event generators this article investigates the impact of such nonperturbative effects on two processes relevant for precision determinations of the strong coupling constant and the proton structure: triple-differential dijet and Z+jet production. We observe significant differences between the two processes. Whether this non-universal behaviour is realized in nature remains an open question. We therefore propose a triple-differential measurement of the underlying event in Z+jet production.

Received 2025-12-01
Accepted 2026-07-02
Published 2026-08-05
Check for updates
doi:10.21468/SciPostPhys.21.2.033

Contents

1 Introduction **1**

2 Analysis phase space **3**

3 Nonperturbative effects **5**
3.1 Dijet production 7
3.2 Z+jet production 7

4 Hadronisation & MPI effects **9**

5 Underlying event analysis **12**
5.1 Analysis 13
5.2 Observations 14

6 Summary and outlook 18
A Generator configurations 19
A.1 HERWIG7 19
A.2 SHERPA 19
B Additional material 19
References 24

1 Introduction

To match the unprecedented precision of measurements at the LHC, accurate predictions of at least next-to-next-to-leading order (NNLO) in perturbative QCD (pQCD) are required. An indispensable ingredient for such calculations are parton distribution functions (PDFs) that describe the manifestly nonperturbative (NP) internal structure of the colliding hadrons and in particular of the proton. Despite significant progress in lattice gauge theory it is not yet possible to derive the proton structure from first principles such that the proton PDFs must be determined in dedicated fits of PDF-dependent observables to precise measurements. Moreover, further NP effects from hadronisation and the Underlying Event (UE) must be estimated by means of Monte Carlo (MC) event generators, since typically the highest-order predictions in pQCD only provide events at parton level.

In this article, NP effects for two processes in proton–proton collisions at the LHC are studied: the inclusive production of dijet events, $p+p \to \text{jet}+\text{jet}+X$, and, generically labelled as Z+jet, the process $p+p \to Z/\gamma^* + \text{jet} + X$, where only the decay channel $Z/\gamma^* \to \mu^+\mu^-$ is considered. For both processes, illustrated in Fig. 1, predictions are available at NNLO accuracy in pQCD [1–5]. While baseline fits of proton PDFs rely on deep-inelastic scattering (DIS) [6], which to first degree depends on the valence quarks and only indirectly on the strong coupling α_s, dijet and Z+jet production both are directly sensitive to α_s and the gluon content of the proton [7–10]. Measurements of these processes at the LHC therefore hold significant potential towards improving the accuracy of α_s and the gluon PDF.

Following the publications by the CMS Collaboration on dijet production at the LHC [12, 13] we choose a setup where the cross section is investigated triple-differentially as a function of the two angular variables y_b and y^* plus one quantity with dimension of energy that correlates with the energy scale of the collision. The two angular variables are defined as

$$y_\text{b} = \frac{1}{2}\left|y_1 + y_2\right| , \tag{1}$$

and

$$y^* = \frac{1}{2}\left|y_1 - y_2\right| , \tag{2}$$

where y_1 and y_2 are the rapidities of the two leading-p_T objects emerging from a collision, i.e. either the leading two jets in dijet production or the reconstructed Z boson and the leading jet in Z+jet events. The quantity y_b corresponds to the longitudinal boost of the centre-of-mass with respect to the laboratory system of a $2 \to 2$ scatter, while y^* is the rapidity of the two back-to-back final-state objects in the centre-of-mass frame. This choice is particularly useful, because the variables y^* and y_b to first order separate the dependence on the partonic scattering angle in the centre-of-mass system from the dependence on the imbalance in the initial-state parton momenta, and hence the PDFs. Moreover, one can derive the following relations to the proton momentum fractions $x_{1|2}$ carried by the incoming partons of a $2 \rightarrow 2$ scatter:

$$\begin{aligned} x_{1|2} &= \frac{2\langle p_{\mathrm{T}}\rangle_{1,2} \cosh(y^*)}{\sqrt{s}} \exp(\pm y_{\mathrm{b}}) \\ &= \frac{m_{1,2}}{\sqrt{s}} \exp(\pm y_{\mathrm{b}})\,. \end{aligned} \tag{3}$$

Here, $\langle p_{\mathrm{T}}\rangle_{1,2}$ and $m_{1,2}$ are the average transverse momentum, $\langle p_{\mathrm{T}}\rangle_{1,2} = (p_{\mathrm{T,jet1}} + p_{\mathrm{T,jet2}})/2$, and the invariant mass, $m_{1,2} = \sqrt{(\mathbf{p}_1 + \mathbf{p}_2)^2}$, of the leading two jets, where $p_{\mathrm{T,jet1}}$, $p_{\mathrm{T,jet2}}$ are their transverse momenta and $\mathbf{p}_1$, $\mathbf{p}_2$ their four-momenta, respectively. Since at leading order (LO) for dijet events $p_{\mathrm{T,jet1}} = p_{\mathrm{T,jet2}} = \langle p_{\mathrm{T}}\rangle_{1,2} = p_{\mathrm{T,jet}}$ and for Z+jet events $p_{\mathrm{T,Z}} = p_{\mathrm{T,jet}}$ we focus in the following on $\langle p_{\mathrm{T}}\rangle_{1,2}$ and $p_{\mathrm{T,Z}}$ as third variable, which we generically label as X. Furthermore, jets are always clustered with the collinear- and infrared-safe anti-k_{T} jet algorithm [14] with a size parameter of $R = 0.4$. Results with respect to the dijet mass, i.e. $X = m_{1,2}$, or for a large jet size parameter of $R = 0.8$ can be found as additional material in Appendix B.

The triple-differential cross section in these three observables can be written in terms of weighted MC events as

$$\frac{d^3\sigma}{dX\,dy_{\mathrm{b}}\,dy^*} = \frac{N_{\mathrm{eff}}(\Delta X, \Delta y_{\mathrm{b}}, \Delta y^*)}{N_{\mathrm{eff,tot}}} \sigma_{\mathrm{incl}}\,, \tag{4}$$

where $N_{\mathrm{eff}}(\Delta X, \Delta y_{\mathrm{b}}, \Delta y^*)$ denotes the effective number of selected events within a given phase space in X, y_{b}, and y^*; $N_{\mathrm{eff,tot}}$ is the effective number of generated events in the full phase space and σ_{incl} is the inclusive cross section for the analysed process. The effective number of events can be expressed in terms of event weights w_i as

$$N_{\mathrm{eff},\mathcal{S}} = \sum_{i \in \mathcal{S}} w_i\,, \tag{5}$$

of the events i within a phase space region $\mathcal{S}$.

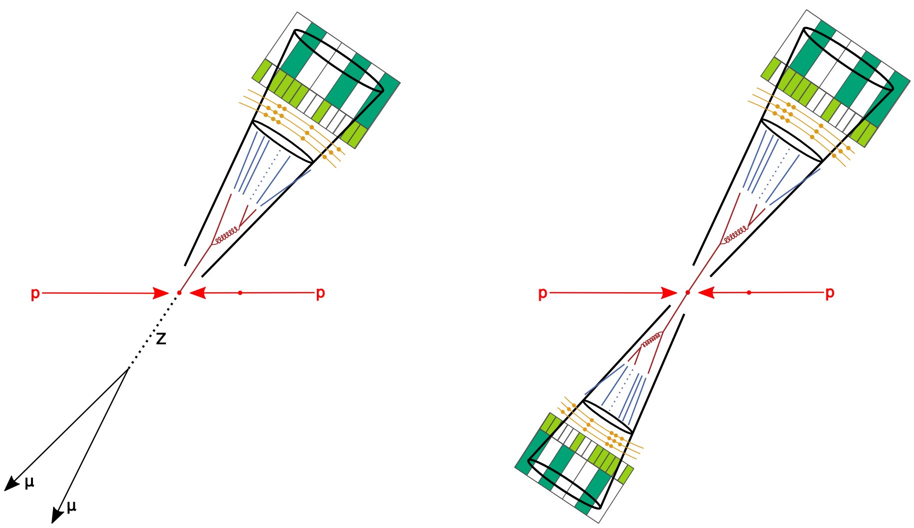

Figure 1: Illustrations of Z+jet (left) [11] and dijet production (right). In the Z+jet case, an oppositely-charged muon pair and at least one jet are required. For the dijet case, a second jet replaces the muon pair.

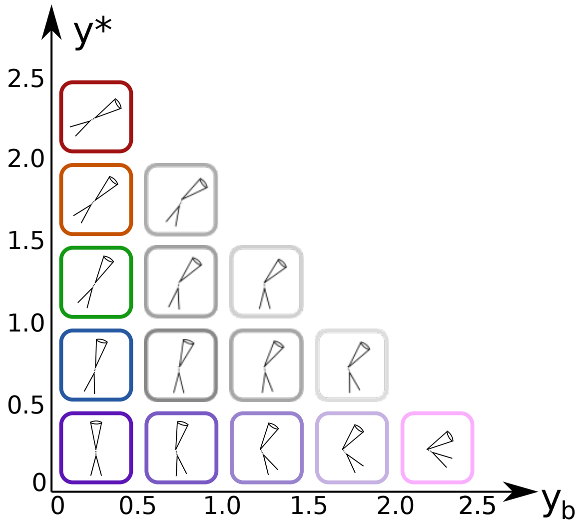

Figure 2: Visualisation of the analysed Z+jet phase space in y_b and y^* as defined in Eqs. 1-2. The bins along the y_b and y^* axes discussed in the main part of this work are indicated by coloured boxes.

This article is organised as follows: Section 2 defines the phase space for the analyses. Nonperturbative corrections for the two investigated processes are derived and discussed in Sect. 3. The separation of NP effects into hadronisation and the Underlying Event is addressed in Sect. 4. A dedicated section 5 examines the behaviour of typical observables for UE studies in the context of the previous section. A summary of the main findings is presented in the concluding Sect. 6. Two appendices provide details on the settings of the MC event generation, App. A, and additional results for $X = m_{1,2}$ as observable or for $R = 0.8$ as jet size parameter, App. B.

2 Analysis phase space

The derived variables y_b and y^* of Eqs. 1 and 2 depend on the rapidities y_1, y_2 of the leading objects measured in a collision event. The latter are constrained by acceptance limitations in the experiments, e.g. ATLAS or CMS [15,16], which can be expressed in terms of the coverage in pseudorapidity η of the relevant subdetectors. For an optimal reconstruction, jets should be measured within coverage of the inner tracking devices extending typically up to $|\eta| \approx 2.5$. Muons can be measured by the ATLAS (CMS) detectors up to $|\eta| = 2.7$ (2.4), leading to a similar constraint on the rapidity y_Z of the Z boson that is reconstructed from an opposite-sign muon pair. The transition from coordinate axes (y_1, y_2) to (y_b, y^*) corresponds to a rotation by $\pi/4$ in rapidity phase space. Applying cuts on (y_1, y_2) leads, after mapping to the first quadrant only, to a triangular-shaped phase space in (y_b, y^*), as illustrated in Fig. 2 for the Z+jet process. Here, we choose a binning scheme for y_b and y^* with a bin width of 0.5 starting from zero up to 2.5. The maximum absolute rapidity allowed for either y_1 or y_2 is given by $y_\mathrm{b} + y^* < |y|_\mathrm{max} = 3.0$, which is slightly larger than the tracker coverage. This results in a total of 15 (y_b, y^*) bins.

In the region where $y_\mathrm{b} < 0.5$, there are five bins ranging from $y^* < 0.5$ to $2.0 \le y^* < 2.5$. Each following y_b region has one y^* bin less than the previous one, finishing with a single bin $y^* < 0.5$ for $2.0 \le y_\mathrm{b} < 2.5$. In the main part of this work, we focus on the nine bins corresponding either to a series of bins with increasing y_b for $y^* < 0.5$, or with increasing y^* for $y_\mathrm{b} < 0.5$ to better showcase our observations. These bins are indicated by coloured

Table 1: The binning scheme in $\langle p_T \rangle_{1,2}$ for the dijet analysis. Due to limited statistical precision, some bins are merged in the edge bins (E) as compared to the central bins (C) in the plane of (y_b, y^*).

Binning scheme	binning labels in (y_b, y^*) plane
(cf. Fig. 2)	E E E C E E C C E E C C C E E
	bin edges in $\langle p_T \rangle_{1,2}$ / GeV
Central (C)	47, 57, 67, 77, 87, 97, 107, 127, 147, 175, 207, 243, 284, 329, 380, 437, 499, 569, 646, 732, 827, 931, 1046, 1171, 1307, 1458, 1621, 1806, 2003, 2217, 2453, 2702
Edge (E)	47, 57, 67, 77, 87, 97, 107, 127, 147, 207, 284, 380, 499, 646, 827, 1046, 1307

boxes in Fig. 2, while results for the remaining bins, drawn with grey boxes, can be found in Figs. 13–16 of Appendix B.

For the final selection criteria and binning of dijet events we follow the publication by CMS [13] and impose $|y|_{max} = 3.0$ for the two leading jets. In contrast to CMS, however, we reduce the $p_{T,jet}$ thresholds from $p_{T,jet1} > 100$ GeV and $p_{T,jet2} > 50$ GeV to 30 GeV and 25 GeV respectively. This allows for an increased overlap in phase space when comparing the dijet and Z+jet processes.

Since the production cross section drops drastically with increasing $\langle p_T \rangle_{1,2}$, the bin widths grow with $\langle p_T \rangle_{1,2}$ to accommodate for the lower expected number of events. Equally, towards outer rapidity the cross section becomes smaller. Therefore, bins in $\langle p_T \rangle_{1,2}$ are merged in nine edge bins (E) at outer rapidities as compared to six central ones (C). The final binning scheme chosen for dijet events is presented in Table 1.

For the Z+jet process, the Z boson is reconstructed from a pair of oppositely charged muons, where the invariant mass of the dimuon system has to be within a range of ±20 GeV around the Z-boson mass $m_Z = 91.1876$ GeV [17]. Muons are considered for an absolute pseudorapidity smaller than 2.4 and a transverse momentum of at least 25 GeV. If multiple Z-boson candidates can be reconstructed, the one closest to m_Z is chosen. The transverse momentum of the reconstructed Z boson has to be at least $p_{T,Z} > 25$ GeV. Jets are required to have a minimum p_T of 20 GeV and an absolute rapidity of less than 2.4. Any jet that overlaps with a prompt muon within $\Delta R(\text{jet}, \mu) < 0.3$ is omitted. The distance ΔR to the muon is defined as

$$\Delta R(\mu, \text{jet}) = \sqrt{\left(\phi_{\text{jet}} - \phi_\mu\right)^2 + \left(\eta_{\text{jet}} - \eta_\mu\right)^2},$$

where ϕ and η are the azimuthal angles and pseudorapidities of the corresponding jet and muon. This ensures that muons, which are also clustered to form jets, are removed from further consideration as “jet”.

Similar to the dijet case, a binning scheme with bin widths increasing with $p_{T,Z}$ and fewer bins in the outer rapidity regions is chosen. Moreover, the suppression of the LO Z+jet process through PDF effects reduces the expected number of events at high y^*, where parton momenta

Table 2: The binning scheme in $p_{\mathrm{T,Z}}$ for the Z+Jet analysis. Due to limited statistical precision, some bins are merged in the edge bins (E) as compared to the central bins (C) in the plane of (y_{b}, y^{*}). An extra wide binning (X) is used for the highest y^{*}-bin.

Binning scheme	binning labels in (y_{b}, y^{*}) plane
(cf. Fig. 2)	X E E C C E C C C E C C C C E
	bin edges in $p_{\mathrm{T,Z}}$ / GeV
Central (C)	25, 30, 35, 40, 45, 50, 60, 70, 80, 90, 100, 110, 130, 150, 170, 190, 220, 250, 400, 1000
Edge (E)	25, 30, 35, 40, 45, 50, 60, 70, 80, 90, 100, 110, 130, 150, 170, 190, 250, 1000
Extra (X)	25, 30, 40, 50, 70, 90, 110, 150, 250

of $x_1 \approx x_2$ are required. As a result, an extra-wide binning (X) is employed for the (y_{b}, y^{*}) bin with $(y_{\mathrm{b}} < 0.5,\ 2.0 \leq y^{*} < 2.5)$. The final binning scheme chosen for Z+jet events is presented in Table 2.

3 Nonperturbative effects

We derive correction factors to fixed-order perturbative calculations for the presented dijet and Z+jet analyses to estimate the size and uncertainty of the effect introduced by the NP models in MC event generators. The full event generation until particle level usually passes through the following steps: the calculation of the perturbative scattering amplitudes and subsequent phase space integration (matrix element, ME), the collinear resummation of leading logarithms with parton showers (PS), the fragmentation of coloured final-state partons into hadrons and subsequent decays of unstable hadrons (Had), and the addition of UE activity via multiple-parton interactions (MPI).

Similar as in previous analyses at the Tevatron or LHC [13, 18–21], the two steps labelled as Had and MPI are considered as NP effects. Hence, we define the NP correction to fixed-order predictions at parton level as the ratio between the nominal predictions with and without hadronisation effects and MPI. The correction at a given perturbative order (PO) of the ME can then be written as:

$$C_{\mathrm{NP}}^{\mathrm{PO}} = \frac{\sigma_{\mathrm{ME+PS+Had+MPI}}^{\mathrm{PO}}}{\sigma_{\mathrm{ME+PS}}^{\mathrm{PO}}}\,, \tag{6}$$

where the subscripts ME+PS+Had+MPI and ME+PS indicate, which steps of the MC event generation have been executed. In other words, the numerator represents the nominal cross section at the particle level given by any MC event generator, while the denominator is the cross section derived from the same MC generator with hadronisation effects and MPI turned off. Because the coloured partons after parton showers can interact with coloured partons stemming from the UE modelling via MPI (colour reconnection), the event generation process must be run twice, once for the numerator and a second time for the denominator leading to statistically independent event samples. As a consequence it is not possible to apply a more elaborate approach using migration matrices for the two levels, although it would certainly be interesting to follow the migration of jets in phase space.

We emphasize that this approach assumes independence of parton shower and hadronization, which certainly is a simplification. There are implicit correlations between parton shower and hadronization, as the parton shower cutoff is an upper scale for the hadronization. When the parton shower is terminated at high scales, the hadronization can compensate for softer radiation that has not been generated by the former, leading to approximately the same total correction. The separate investigation of the two effects, however, may include a residual effect of this correlation. Nevertheless, we follow the conventional procedure to quantify non-perturbative effects in experimental analyses to date.

For an automated and scalable generation of the MC events and subsequent analysis, the MCRun software framework [22] based on the workflow management tool LAW [23] is used. The LAW package implements and calls the tasks related to the necessary code executions, automatically resolves their dependencies, and manages and distributes the computational payloads on available computing resources. The configurations used for the results in this work are made available within the MCRun software allowing for an efficient reproduction of the same workflow. A dedicated Rivet [24] routine for each process, respectively, analyses event records produced by the two MC event generators Herwig7 version 7.2.3 [25, 26] and Sherpa version 2.2.15 [27]. An overview of the generator settings for all samples generated with Herwig7 is given in Table 3 of Appendix A.1 and in Table 4 of Appendix A.2 for the Sherpa samples. Jets are clustered utilising the FastJet [14, 28] library. Selection cuts based on reconstructed objects, as described in the previous Sect. 2, are applied, and fiducial cross sections for each differential bin are calculated. These cross sections are computed for event generations up to particle (full) and parton level only (partial). Finally, NP correction factors are calculated following Eq. 6 from the obtained cross sections for each bin.

The obtained correction factors C_{NP} are subject to statistical fluctuations due to the limited number of generated events in both the full and partial generation sequences. To smooth these fluctuations, the NP correction is parameterised using an interpolating function

$$f(x) = a \cdot \ln(x/\mathrm{GeV})^b + c\,, \tag{7}$$

in each (y_{b}, y^*) bin. This parameterisation is chosen, since the NP effects are expected to contribute in phase-space regions where the typical energy of the collision approaches hadronic energy scales while fading out towards higher energies. Since the third observable is correlated with the energy scale of the collision process, we expect to see larger NP effects towards lower values of X, while the NP correction factors should approach unity towards high X. Indeed, the fitted values for the parameter c are compatible with unity and the obtained fits match the MC simulation well supporting these expectations independent of the analysed topology, perturbative order, or (y_{b}, y^*) bin.

3.1 Dijet production

The triple-differential dijet cross section is measured as a function of the three observables y_{b} and y^*, as defined in Eqs. 1-2, and either the average transverse momentum $\langle p_{\mathrm{T}}\rangle_{1,2}$ or the mass $m_{1,2}$ of the dijet system. The resulting NP correction factors derived with Herwig7 at LO and next-to-leading order (NLO) [25, 26, 29, 30] accuracy in pQCD of the ME are shown in Fig. 3 for anti-k_{T} jets with $R = 0.4$ in the selected (y_{b}, y^*) bins. Further bins can be found in Appendix B in Fig. 13 together with correction factors for dijet production vs. the dijet invariant mass $m_{1,2}$ of the leading and subleading jet. NP correction factors for anti-k_{T} jets with radius parameter $R = 0.8$ can be found in Fig. 14 of the same appendix.

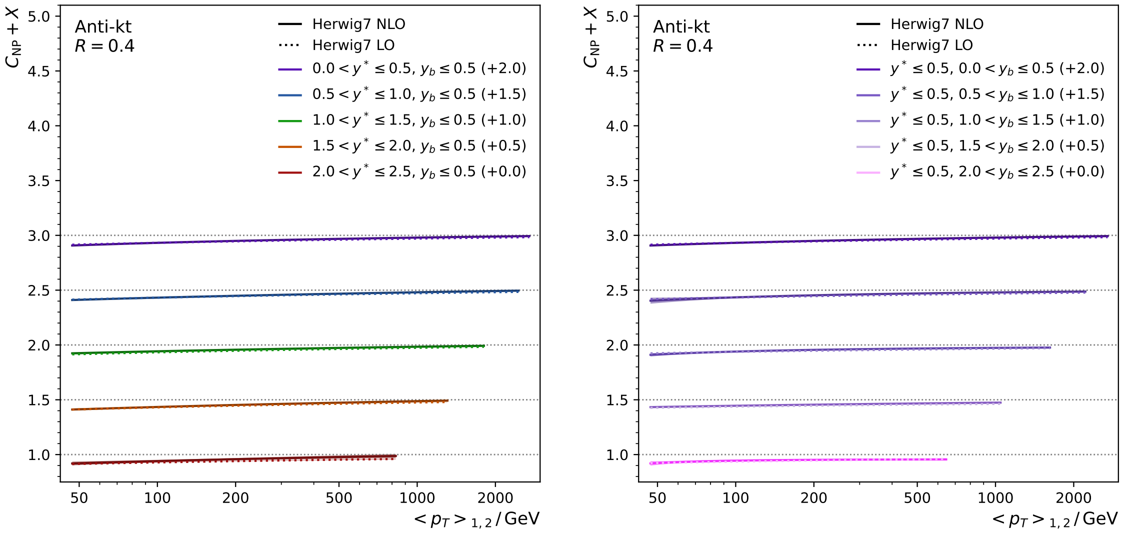

Figure 3: C_{NP} vs. dijet $\langle p_{\mathrm{T}}\rangle_{1,2}$ using LO (dotted) and NLO MEs (solid lines) in HERWIG7 predictions for anti-k_{T} jets with $R = 0.4$. Bands indicate the statistical uncertainty. The fitted curves are shown for a series of phase space intervals increasing in y^* for $y_{\mathrm{b}} < 0.5$ (left) and increasing in y_{b} for $y^* < 0.5$ (right). The factors are shifted with respect to unity by constant offsets.

The observed correction factors for dijet production are close to unity for large $\langle p_{\mathrm{T}}\rangle_{1,2}$ ($m_{1,2}$) and decrease towards small $\langle p_{\mathrm{T}}\rangle_{1,2}$ ($m_{1,2}$) as expected. They exhibit no significant dependence on the perturbative order or (y_{b}, y^*) bin.

3.2 Z+jet production

This process can be measured triple-differentially in a similar fashion as the dijet production. The observable that quantifies the scale of the hard interaction is chosen to be the transverse momentum of the muon pair, labelled as $p_{\mathrm{T,Z}}$ in the following:

$$p_{\mathrm{T,Z}} = \left|\vec{p}_{\mathrm{T},\mu^-} + \vec{p}_{\mathrm{T},\mu^+}\right| , \tag{8}$$

where $\vec{p}_{\mathrm{T},\mu^-}$ and $\vec{p}_{\mathrm{T},\mu^+}$ are the transverse momenta of the muon pair forming the Z-boson candidate. The rapidity observables y_{b} and y^* are defined analogously to Eqs. 1-2 with y_1 being the rapidity of the Z boson, y_{Z}, and y_2 corresponding to the rapidity of the leading jet in the event y_{jet1}.

NP correction factors derived with HERWIG7 at LO and NLO accuracy in pQCD[1] are presented in Fig. 4 for anti-k_{T} jets with $R = 0.4$ for the selected (y_{b}, y^*) bins. Further (y_{b}, y^*) bins as well as all bins for anti-k_{T} jets with $R = 0.8$ can be found in Figs. 15–16 in Appendix B. In contrast to the behaviour observed for dijet production, we find a trend towards larger correction factors with rising y^* but not with rising y_{b}. This trend in y^* seems to be somewhat reduced using NLO MEs, where all NP correction factors exhibit an overall decrease in magnitude as compared to LO MEs.

As a cross-check, the NP correction factors derived using HERWIG7 are compared in Fig. 5 to SHERPA [27, 31] at LO and NLO accuracy. The NP corrections derived with SHERPA are overall larger than the ones predicted by HERWIG7. The general features, however, of smaller corrections at NLO than at LO and the y^* dependence are reproduced by SHERPA.

[1]Here, leading and next-to-leading order explicitly require the production of at least one jet in addition to the Z boson: Z+jet+X.

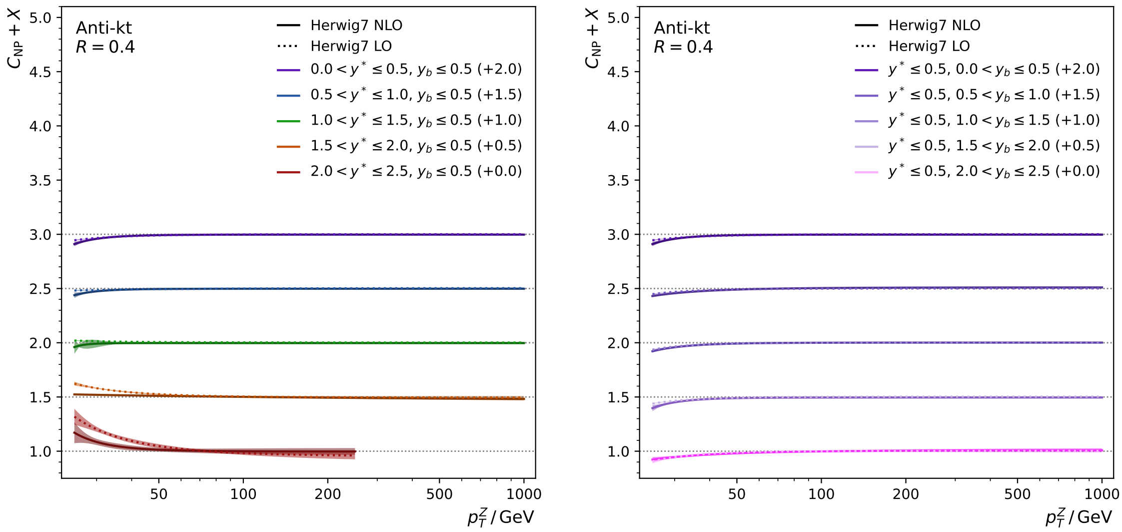

Figure 4: Same as Fig. 3 but vs. $p_{\mathrm{T,Z}}$ in Z+jet production.

To verify the trend observed with increasing parton multiplicity at ME level, NP correction factors with multi-leg merged Z+jet with zero and one jet at NLO, and with two and three jets at LO ME accuracy are generated using SHERPA. The corresponding NP correction factors are shown in Fig. 6. Again a similar dependence on y^* is visible in the NP correction factors derived from the multi-leg merged Z+jet event sample. Also, the behaviour of overall smaller NP corrections with higher multiplicity in the ME for the event generation is confirmed. Consistently, no dependence on y_{b} is observed.

This dependence of the NP correction factors on y^* and on the perturbative order of the MEs in generating the hard amplitudes indicates that part of the observed NP correction factors might, in fact, originate in the perturbative modelling. The labelling as “nonperturbative” might therefore not be completely appropriate. Interestingly, smaller NP corrections with NLO+PS MC event generators as compared to LO+PS and rapidity-dependent PS effects have previously been reported in the context of inclusive jet production binned in jet p_{T} and absolute rapidity in Refs. [20, 32]. Furthermore, the fact that this y^* dependence is only observed for the Z+jet but not for the dijet process motivates a more thorough investigation.

4 Hadronisation & MPI effects

According to our definition the NP correction factors account for two effects, hadronisation and the UE, which we attempt to study individually in the following.

The parton final state is determined by the parton showers that produce additional, visible activity in all hard events. This also holds for the additional events from MPI that are superimposed with the primary hard events. After the parton showers, all partons in the final state are assigned a colour line, which in turn assigns a colour partner to each parton. This would lead to uncorrelated events from MPI and to a strong growth of charged particle multiplicity with the number of additional hard events. However, the observation of increasing average transverse momentum in higher multiplicity events necessitates colour reconnection (CR) models that lead to interference between the coloured final states of the primary hard events and the MPI events.

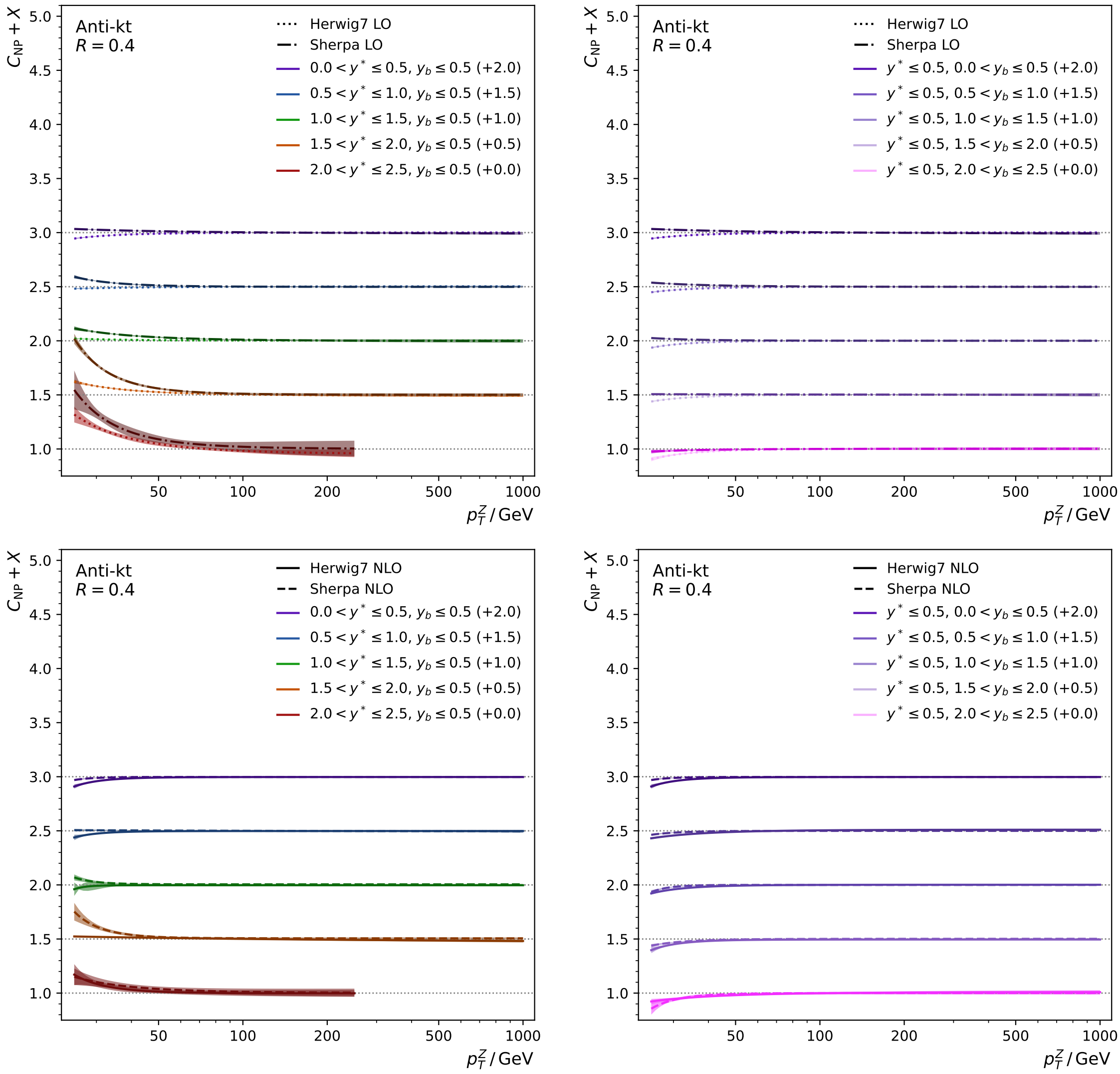

Figure 5: Comparison of C_{NP} vs. $p_{T,Z}$ between HERWIG7 (dotted & solid lines) and SHERPA predictions (dash-dotted & dashed lines) using LO (top row) and NLO MEs (bottom row) for anti-k_T jets with $R = 0.4$. Bands indicate the statistical uncertainty. The fitted curves are shown for a series of phase space intervals increasing in y^* for $y_b < 0.5$ (left) and increasing in y_b for $y^* < 0.5$ (right). The factors are shifted with respect to unity by constant offsets.

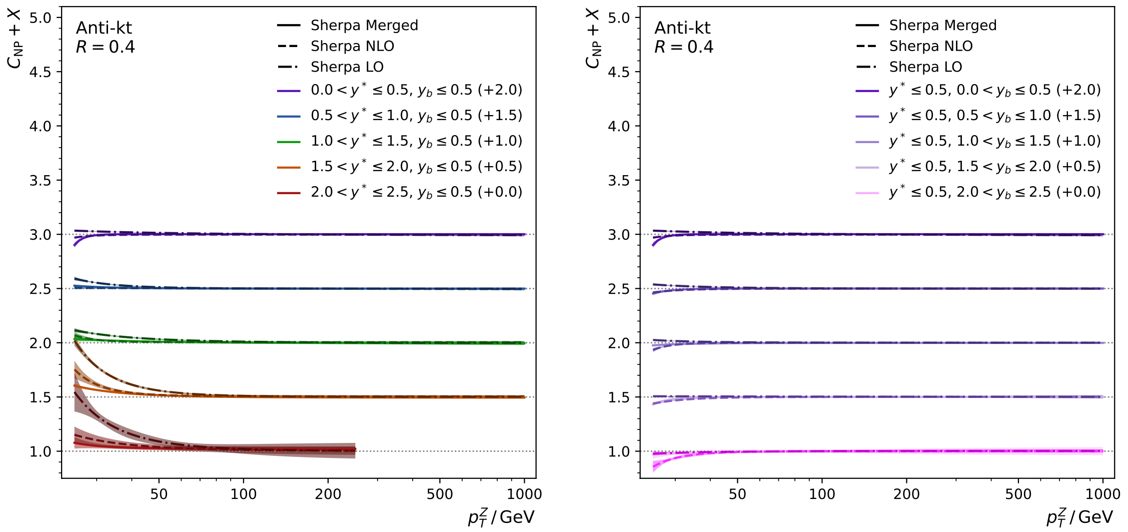

Figure 6: Comparison of C_{NP} vs. $p_{\mathrm{T,Z}}$ among SHERPA predictions using LO (dash-dotted), NLO (dashed), and multi-leg merged MEs (solid lines) for anti-k_{T} jets with $R = 0.4$. Bands indicate the statistical uncertainty. The fitted curves are shown for a series of phase space intervals increasing in y^* for $y_{\mathrm{b}} < 0.5$ (left) and increasing in y_{b} for $y^* < 0.5$ (right). The factors are shifted with respect to unity by constant offsets.

The modelling of colour reconnection is based on the idea of colour pre-confinement, i.e. the observation that partons that are close to each other in phase space (usually momentum space) tend to exchange soft, NP gluons in a way that their colour lines are reconnected to become partners with close neighbours. While there are ideas to put this on a firm theoretical basis of a colour evolution model [33–35], most modern event generators still model this effect by minimising a "colour distance" of neighbouring partons [36–38]. For our consideration, which is purely based on observations of the final state, we should simply keep in mind that colour reconnection also links the MPI with the hadronisation models that we took as signposts for the NP modelling.

In order to nonetheless get an approximate, individual handle on the hadronisation and MPI effects, respectively, we compute hadronisation and MPI correction factors similar to Eq. 6 as

$$C_{\mathrm{Had}}^{\mathrm{PO}} = \frac{\sigma_{\mathrm{ME+PS+Had}}^{\mathrm{PO}}}{\sigma_{\mathrm{ME+PS}}^{\mathrm{PO}}}, \tag{9}$$

and

$$C_{\mathrm{MPI}}^{\mathrm{PO}} = \frac{\sigma_{\mathrm{ME+PS+MPI}}^{\mathrm{PO}}}{\sigma_{\mathrm{ME+PS}}^{\mathrm{PO}}}. \tag{10}$$

The hadronisation correction factors C_{Had} for Z+jet production with anti-k_{T} jets with radius parameter $R = 0.4$ computed with HERWIG7 at LO and NLO accuracy in pQCD of the ME are shown in Fig. 7. They are consistently approaching a value of unity for high $p_{\mathrm{T,Z}}$. Towards small $p_{\mathrm{T,Z}}$ the downwards deviation from unity increases as expected for out-of-cone effects through hadronisation. However, they show no significant dependence on y_{b}, y^* or the perturbative order of the generated samples.

On the contrary, the corresponding MPI correction factors C_{MPI} for Z+jet production computed with HERWIG7, shown in Fig. 8, reveal trends versus y^* and the perturbative order resembling the ones observed for the NP correction factors in Sect. 3. They also approach unity towards high $p_{T,Z}$, while for small $p_{T,Z}$ this time the upwards deviation from unity increases reflecting a higher share of MPI partons migrating into a jet. The magnitude of the increase towards small $p_{T,Z}$ correlates with y^* and decreases with increasing perturbative order. These observations indicate that the origin of the observed trends for the NP correction factors lies, at least partially, in the MPI model.

5 Underlying event analysis

As observed in Sect. 4, both hadronisation and the UE each play a role for the NP corrections. Although these two effects cannot be completely decoupled, the trends with y^* and the perturbative order in the NP correction factors noticed in Sect. 3 must mainly originate from MPI effects.

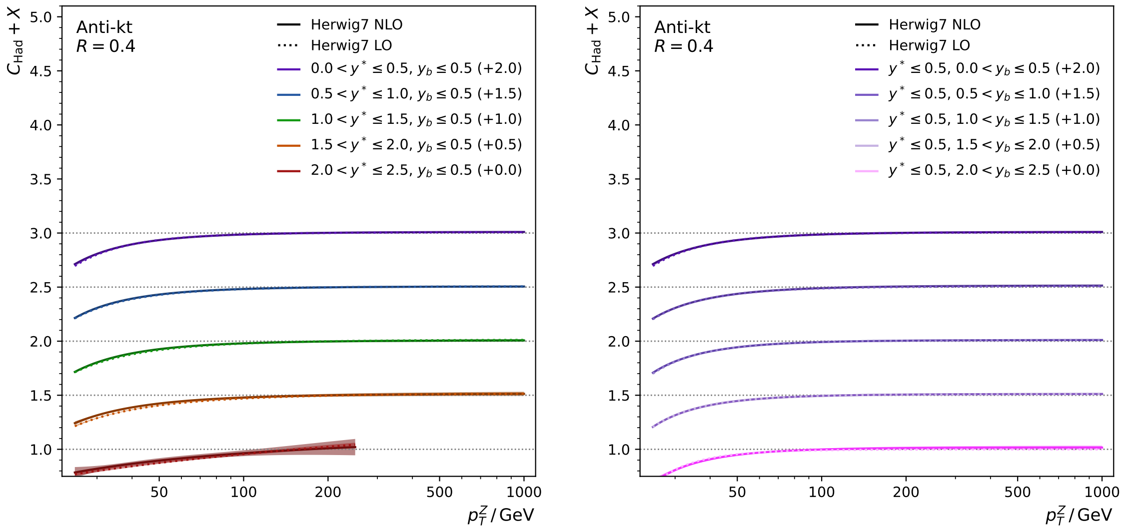

Figure 7: Same as Fig. 4 but for hadronisation effects, C_{Had}, only.

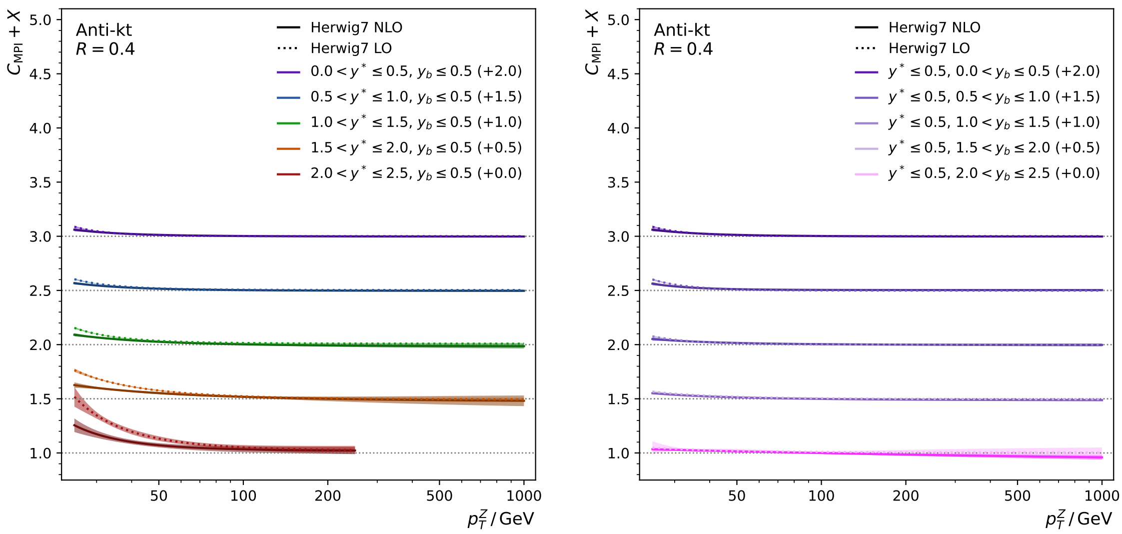

Figure 8: Same as Fig. 4 but for MPI effects, C_{MPI}, only.

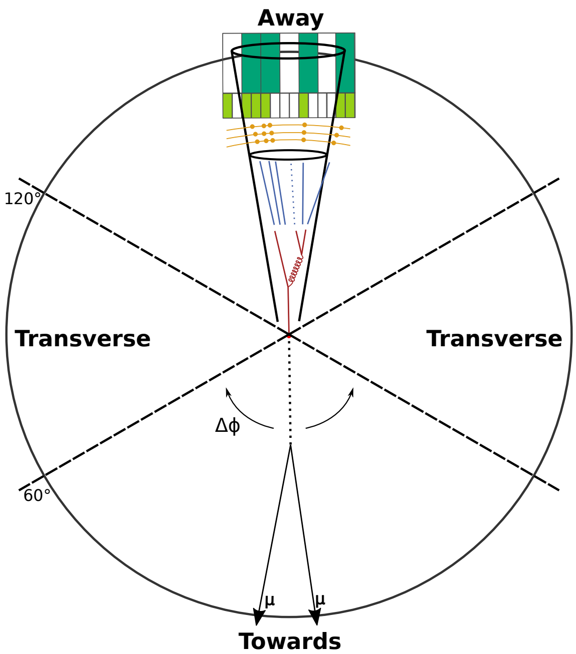

Figure 9: Visualisation of the analysed phase space for the UE analysis. The away, towards, and transverse regions are defined relative to the direction in azimuthal angle ϕ of the dimuon system.

In this section, a closer look at the NP effects, focusing especially on MPI, is presented. For this purpose, observables of "Rick-Field-type" UE analyses are utilised that are typically employed as sensitive observables in tuning and modelling studies [39–41].

5.1 Analysis

We pre-select Z+jet events as in the previous sections in bins of y_{b} and y^*, however, with two modifications for the UE analysis: First, there is no minimum $p_{\mathrm{T,Z}}$ required, and secondly only charged particles are considered for the UE observables. Moreover, the p_{T} of each such particle must exceed 500 MeV. Then, the momentum of the lepton pair, i.e. the Z boson, is chosen to define the direction of the leading particle and henceforth the origin of the azimuthal angle ϕ for the UE analysis. All other charged particles, including the ones from the jet, are categorised as belonging to one of three azimuthal regions, depending on the azimuthal angular difference $\Delta\phi$ relative to the leading particle, such that $-\pi < \Delta\phi \leq \pi$. Particles with $|\Delta\phi| \leq \pi/3$ are in the *towards* region, moving roughly forward relative to the leading particle. Particles moving in the direction of the recoiling jet, defined by $|\Delta\phi| > 2\pi/3$, are assigned to the *away* region. The remaining region with $\pi/3 < |\Delta\phi| \leq 2\pi/3$ is called the *transverse* region. Figure 9 illustrates the three regions relative to the (downwards-going) leading particle and the recoiling jet.

In a dijet or minimum bias event, the transverse region allows us to have a closer look at those particles that are furthest away from the leading, hard interaction. These particles are associated with the UE activity, as it is observed that, beyond a certain threshold, the activity in the UE is more or less decorrelated from the hard interaction. In order to quantify the activity of the UE, two different observables are considered in bins of different "hardness" of the leading particle characterised by its transverse momentum. For a given leading-particle transverse momentum, the average number of charged particles N_{ch} or the sum of absolute transverse momenta $\sum p_T^{\mathrm{ch}}$ in either of the previously defined regions are considered as a measure for the activity in these regions.

In dijet or minimum bias events, the activity in the towards and away region is strongly associated with the transverse momentum of the leading particle. Hence, both observables tend to grow with increasing hardness of the event. The parton radiation associated with the hardness of the event will mostly populate the towards and away region, but can spill over into the transverse region. If there is a portion of the event that is more or less uncorrelated to the hard event, as it is modelled in most MPI models, the activity in the transverse region should be dominated by the MPI activity or at least be the region that is least overshadowed from particles associated with the hard event.

In events with the Z boson as the leading particle, this is somewhat different. The hardness of the event is associated with the transverse momentum of the Z boson. With increasing transverse momentum of the Z boson the recoiling activity will mostly be in the away region, while the region around the lepton pair, i.e. the towards region, should be the one with the least activity from the UE.

In this work, it is of interest whether the large NP corrections for relatively low transverse momentum of the Z boson, particularly for increasing values of y^*, are really related to the activity from MPI. In these events, where the Z boson and the recoiling jet are getting closer and closer to the beam axis, there might also be a strong influence from parton radiation around the beam direction. Therefore, the UE observables are studied with different generators and for different matching and merging scenarios in order to discriminate activity due to hard radiation in the event from MPI activity.

5.2 Observations

To illustrate our findings, plots of the activity $\sum p_T^{\text{ch}}$ in the three different regions are shown. The results for N_{ch} are qualitatively similar and therefore omitted in this discussion. These observables are derived from events generated with HERWIG7 and SHERPA with both LO and NLO accuracy of the hard Z+jet process. In addition, results obtained from the multileg-merged samples from SHERPA are compared.

The description of UE observables in inclusive Z+jet events with HERWIG7 has been considered before and is known to give a reasonable agreement with data [41–45]. We therefore focus on the UE observables in differential (y_b, y^*) bins as defined in Sec. 2. In the following discussions, the outermost y^* bin $(2.0 \leq y^* < 2.5)$ is omitted, because it is subject to large statistical fluctuations.

In Fig. 10 from top to bottom the results from LO ME event generation for the activity in the three regions away, towards and transverse are shown. In the left column y_b is fixed to the central bin $(y_\text{b} < 0.5)$, while y^* is varied. In the right column the respective results with y^* fixed, while y_b varies, are shown. It is apparent that the UE activity varies strongly with y^* while there is no apparent variation with y_b. In the simplified back-to-back picture this means that the activity increases only when the central back-to-back hard event is tilted with y^* but not when a central back-to-back hard event is boosted along the beam axis. The naïve expectation is that any contamination of activity from the beam or MPIs should occur in both situations likewise. Instead, the increased activity with y^* in all regions hints at some relation between the hard event topology and the observed UE activity.

Considering the away region, it is found that the activity here is strongly correlated with the transverse momentum of the Z boson and increases with y^*. This reflects mostly the activity in the recoiling jet, which for increasing y^* pulls in more particles from the beam direction. Also, we can clearly see that, as expected, the activity in this region increases significantly from around 20 GeV, which is the selection cut for the jet itself. Below 20 GeV in $p_{\text{T,Z}}$ the p_T of the "balancing" jet must be compensated by other hadronic activity in the towards region. In fact, the hadronic activity in the towards and transverse regions decrease slightly from $p_{\text{T,Z}} = 7.5\,\text{GeV}$ up to 20 GeV. Increasing y_b at central y^* in Fig. 10 (right column) does not exhibit significant changes in activity in any region.

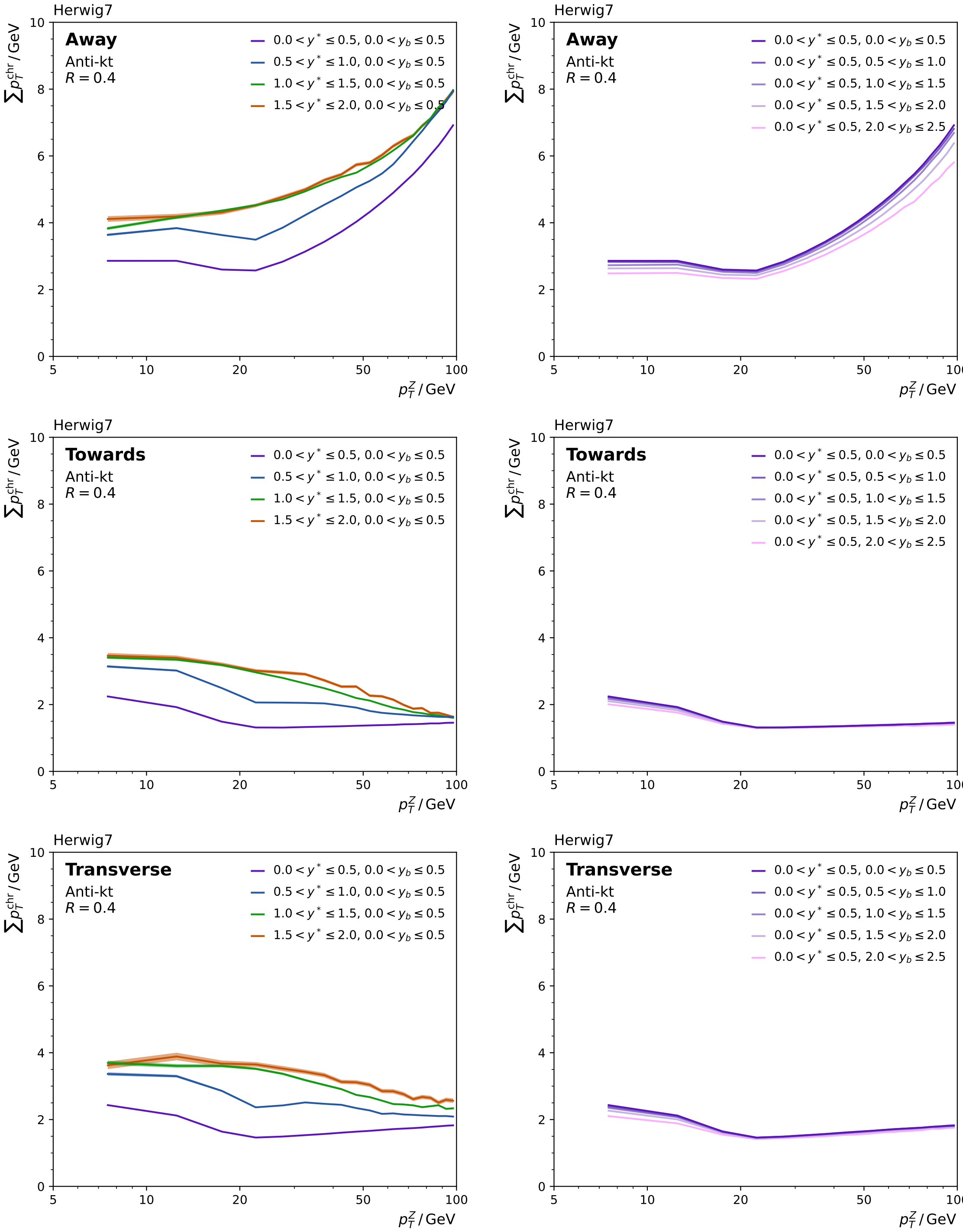

Figure 10: Comparison of the sum of transverse momenta of all charged particles, $\sum p_T^{\text{chr}}$, in bins of $p_{\text{T,Z}}$, y_{b}, and y^* for the away (top), towards (middle), and transverse region (bottom row) as predicted by HERWIG7 using LO MEs for event generation up to particle level. The values are shown for a series of phase space intervals increasing in y^* for $y_{\text{b}} < 0.5$ (left) and increasing in y_{b} for $y^* < 0.5$ (right).

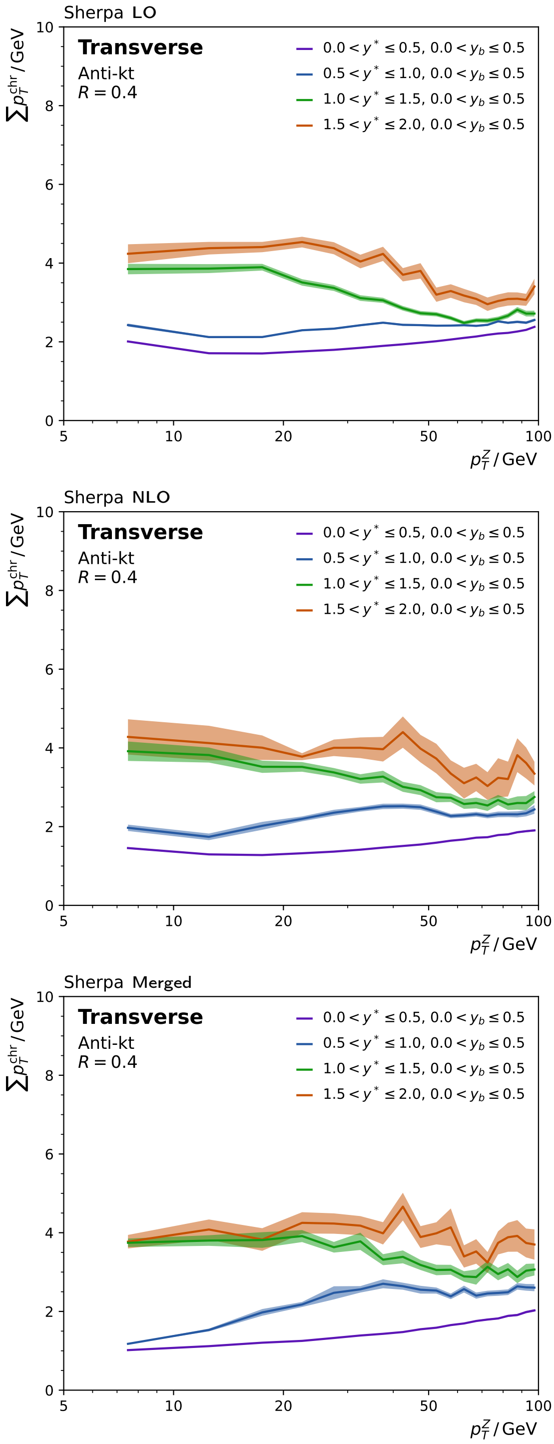

Figure 11: Comparison of the sum of transverse momenta of all charged particles, $\sum p_T^{\mathrm{chr}}$, for central y_{b} in bins of $p_{\mathrm{T,Z}}$ and y^* for the transverse region as predicted by SHERPA using LO (top), NLO (middle), and multileg-merged MEs (bottom) for event generation up to particle level.

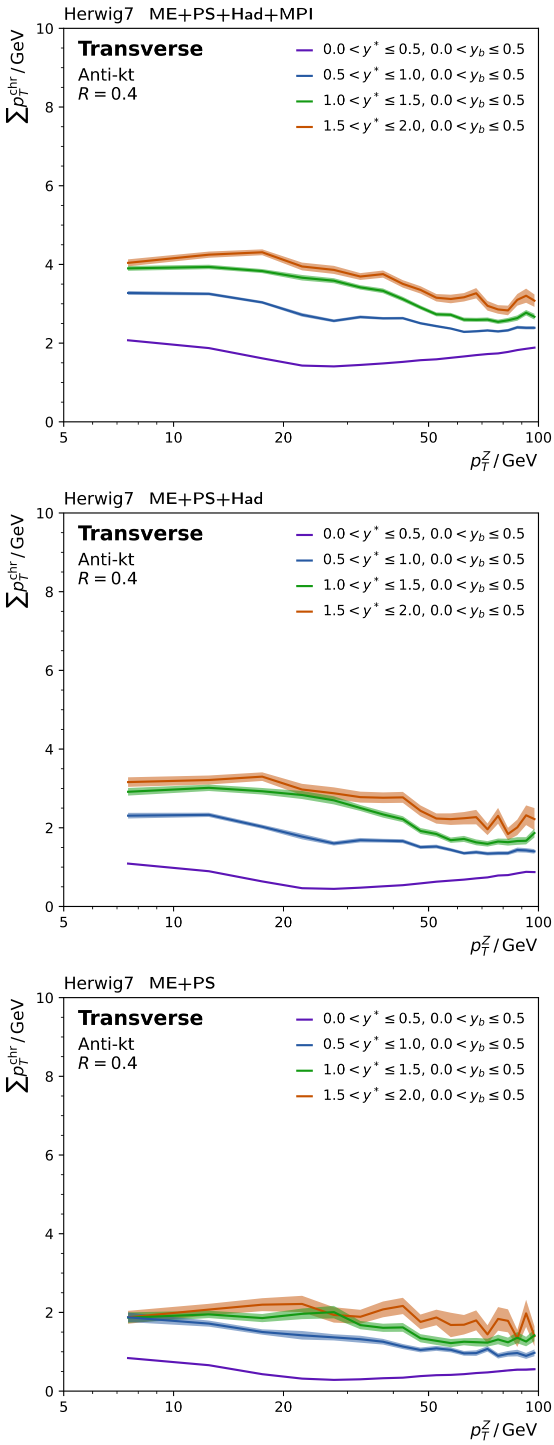

Figure 12: Comparison of the sum of transverse momenta of all charged particles, $\sum p_T^{\text{chr}}$, for central y_b in bins of $p_{\text{T,Z}}$ and y^* for the transverse region as predicted by HERWIG7 using NLO MEs for event generation up to particle level with MPI (top), without MPI (middle), and up to parton level only, i.e. hadronisation and MPI off (bottom).

Two cross-checks are performed. First, HERWIG7 was used with a hard process at NLO instead of LO accuracy (not shown). Generally, the results are similar to the LO case. In particular, only a dependence on y^* is observed but not on y_b. The activity in the transverse region is slightly lower at NLO than at LO. Secondly, SHERPA was employed with the ME at LO, NLO, and with multi-leg merging as shown for the transverse region in Fig. 11. As with HERWIG7 the UE activity in the transverse region strongly depends on y^* but not on y_b, and decreases slightly with a more accurate simulation of the hard event.

Finally, in Fig. 12 the same NLO simulation with HERWIG7 with the full generation up to particle level is compared to two partial generation chains. More specifically, first, only the MPI is turned off (ME+PS+Had), and secondly both the MPI and hadronisation (ME+PS) are switched off. In comparison to the full generation mostly the overall normalisation changes suggesting the effect, that the MPI essentially adds activity to the event, but remains broadly uncorrelated with the hard event, as does hadronisation. In summary, hadronisation and MPI alone cannot fully explain the y^* dependence and perturbative effects significantly contribute as well.

6 Summary and outlook

We find that nonperturbative (NP) corrections for Z+jet events in the triple-differential measurement of the cross section strongly depend on the scattering angle of the hard process in the centre-of-mass frame, y^*, but barely on the boost of the hard scatter, y_b. The event generation with hadronisation effects switched off hinted at the Underlying Event (UE) simulation as being responsible for this extra activity. However, looking into this effect with the help of a typical UE analysis in the same triple-differential binning has shown that a substantial part of the extra activity must be of perturbative origin. The UE analysis shows the same strong dependence on y^*, even when the multiple parton interactions (MPI) as a model for the UE are switched off. Albeit this UE observable has not yet been measured triple-differentially, we find consistency between the simulation with the event generators HERWIG7 and SHERPA. In contrast, the NP correction factors for the dijet case do not exhibit this strong dependence on y^*.

In summary, we find that NP corrections, derived in the conventional way as defined in Eq. 6, may not be entirely of NP origin. Moreover, they are not universal among different hard processes. The inclusion of unobserved jets will lead to additional activity that should not be attributed to non-perturbative effects but alter the correction factors by a possibly large amount. In our specific case this means that in order to simulate the corrections for Z+jets one should include a number of additional jets via multijet merging, possibly at NLO, in order to obtain appropriate correction factors. Furthermore, to clarify the observation of the y^* dependent UE activity in Z+jet event, we recommend measuring the UE activity triple-differentially.

Acknowledgments

We thank Simon Plätzer for fruitful discussions during early stages of this work.

Funding information This work was supported by the German Federal Ministry of Education and Research (project funding numbers 05H2021, 05H21GUCC2, 05H21VKCCA). The authors also acknowledge support by the state of Baden-Württemberg through bwHPC and the German Research Foundation (DFG) through grant no INST 39/963-1 FUGG (bwForCluster NEMO).

A Generator configurations

In the following, a summary of the generation settings for HERWIG7 and SHERPA are given that have been used to generate the samples used in this work. Their complete configurations can be found in the utilized steering files published in the `inputfiles` directory of the software framework MCRUN [22].

A.1 HERWIG7

An overview of the generator settings for all samples generated with HERWIG7 is given in Table 3. The samples in the table are labelled according to the underlying process and the perturbative accuracy in QCD they are generated with. For reference, the respective tree-level process with the orders of the QCD and electro-weak coupling constants are given.

At the lowest final state multiplicity, the dijet samples contain events with at least two partons at ME level, the Z+jet events contain an oppositely charged muon pair and one jet. Further settings for the matrix element generation are the lower transverse momentum cutoff for the coloured final state particles labelled as $k_T^{\text{jet,min}}$, the choice of the renormalization and factorization scales, and the chosen PDF sets. Both scales are set for the dijet case to the transverse momentum of the hardest parton $\max(p_T^{\text{jet}})$ and for the Z+jet case to the invariant mass of the oppositely charged muon pair $m_{\mu^+\mu^-}$. All are interfaced to the angular ordered parton shower in HERWIG7 [25, 26] and the NLO samples are matched to the parton shower by HERWIG7's own implementation of the MC@NLO matching algorithm [25, 26, 46].

The dijet samples are generated with the non-perturbative models tuned to the CH3 set of parameters [47] based on the default tune that comes predefined with HERWIG7. The Z+jet samples are generated without any changes to the MPI model parameters compared to the default tune that comes with HERWIG7 version 7.2.

A.2 SHERPA

For the samples generated with SHERPA an overview of the generator settings is given in Table 4. They are labelled following the same logic and the overall information given in the table and its structure follows what is given in the HERWIG7 case described in Appendix A.1.

At ME level the LO and NLO Z+jet samples contain events with a oppositely charged dimuon pair plus one jet at the lowest multiplicity. The factorization and renormalization scales are dynamically determined with the `SCALES METS` scheme. In all cases the generated events are interfaced to the CSS parton shower [48]. The NLO real corrections at the ME level in the NLO sample are matched to the parton shower using SHERPA's implementation of the MC@NLO algorithm [49]. In the Merged case contributions from MEs with 0, 1, 2, and 3 partons are merged and interfaced with the parton shower using the MEPS@NLO [50, 51], for zero and one, and the MENLOPS [52, 53] techniques, for two and three partons, with a merging cut $Q_{\text{cut}} = 15\,\text{GeV}$. In the LO and NLO generations, the merging cut $Q_{\text{cut}} = 15\,\text{GeV}$ serves as the regulating cut for the parton emission.

The default tunes of the non-perturbative models shipped with SHERPA version 2.2.15 have been utilized in the generation of all samples.

B Additional material

In this section additional results are presented for all phase space intervals in (y_b, y^*) and for the two jet size parameters $R = 0.4$ and 0.8. Figures 13 and 14 show the NP correction factors as derived from HERWIG7 with LO and NLO MEs for dijet production versus $\langle p_T \rangle_{1,2}$ and $m_{1,2}$.

The binning scheme for dijet mass is given in Table 5, which, in contrast to $\langle p_{\mathrm{T}}\rangle_{1,2}$, has not been extended to include results at lower p_{T}. Furthermore, Figures 15 and 16 show the NP correction factors as derived from HERWIG7 and SHERPA for all available perturbative orders of the MEs for Z+jet production versus $p_{\mathrm{T,Z}}$.

Lacking a physics-related motivation for the smoothing function of the NP corrections at low scales, it should be noted that the derived curves are valid only within the shown range and should not be extrapolated. In particular, when the inset of a steeper increase (or decrease) versus lower values of $\langle p_{\mathrm{T}}\rangle_{1,2}$, $m_{1,2}$, or $p_{\mathrm{T,Z}}$ is represented by only one bin at the low edge, statistical fluctuations may lead to exaggerated slopes.

Table 3: Generator settings for the samples generated with HERWIG7 version 7.2.3.

Process Label	tree-level MEs	$\mathcal{O}(\alpha_s), \mathcal{O}(\alpha)$	$k_T^{\mathrm{jet,min}}$	scales	PDF set	PS	Matching/Merging	Tune
dijet LO	$p+p \to j+j$	2, 0	20 GeV	$\max(p_T^{\mathrm{jet}})$	NNPDF31_nnlo_as_0118	AO	–	CH3
dijet NLO	$p+p \to j+j$	2, 0	20 GeV	$\max(p_T^{\mathrm{jet}})$	NNPDF31_nnlo_as_0118	AO	MC@NLO	CH3
Z+jet LO	$p+p \to \mu^+ + \mu^- + j$	1, 2	20 GeV	$m_{\mu^+\mu^-}$	CT14lo	AO	–	Default
Z+jet NLO	$p+p \to \mu^+ + \mu^- + j$	1, 2	20 GeV	$m_{\mu^+\mu^-}$	CT14nlo	AO	MC@NLO	Default

Table 4: Generator settings for the samples generated with SHERPA version 2.2.15.

Process Label	tree-level MEs	$\mathcal{O}(\alpha_s), \mathcal{O}(\alpha)$	Q_{cut}	scales	PDF set	PS	Matching/Merging	Tune
Z+jet LO	$p+p \to \mu^+ + \mu^- + j$	1, 2	15 GeV	SCALES METS	CT14lo	CSS	–	Default
Z+jet NLO	$p+p \to \mu^+ + \mu^- + j$	1, 2	15 GeV	SCALES METS	CT14nlo	CSS	MC@NLO	Default
Z+jet Merged	$p+p \to \mu^+ + \mu^- \{+j+j+j\}$	0, 2	15 GeV	SCALES METS	CT14nlo	CSS	MEPS@NLO (0,1 jets), MENLOPS (2,3 jets)	Default

Table 5: The binning scheme in $m_{1,2}$ for the dijet analysis. Due to limited statistical precision, some bins are merged in the edge bins (E) as compared to the central bins (C) in the plane of (y_{b}, y^*).

Binning scheme	binning labels in (y_{b}, y^*) plane
(cf. Fig. 2)	E E E C E E C C E E C C C E E
	bin edges in $m_{1,2}$ / GeV
Central (C)	306, 372, 449, 539, 641, 756, 887, 1029, 1187, 1361, 1556, 1769, 2008, 2273, 2572, 2915, 3306, 3754, 4244, 4805, 5374, 6094
Edge (E)	372, 539, 756, 1029, 1361, 1769, 2273, 2915, 3754, 4805, 6094

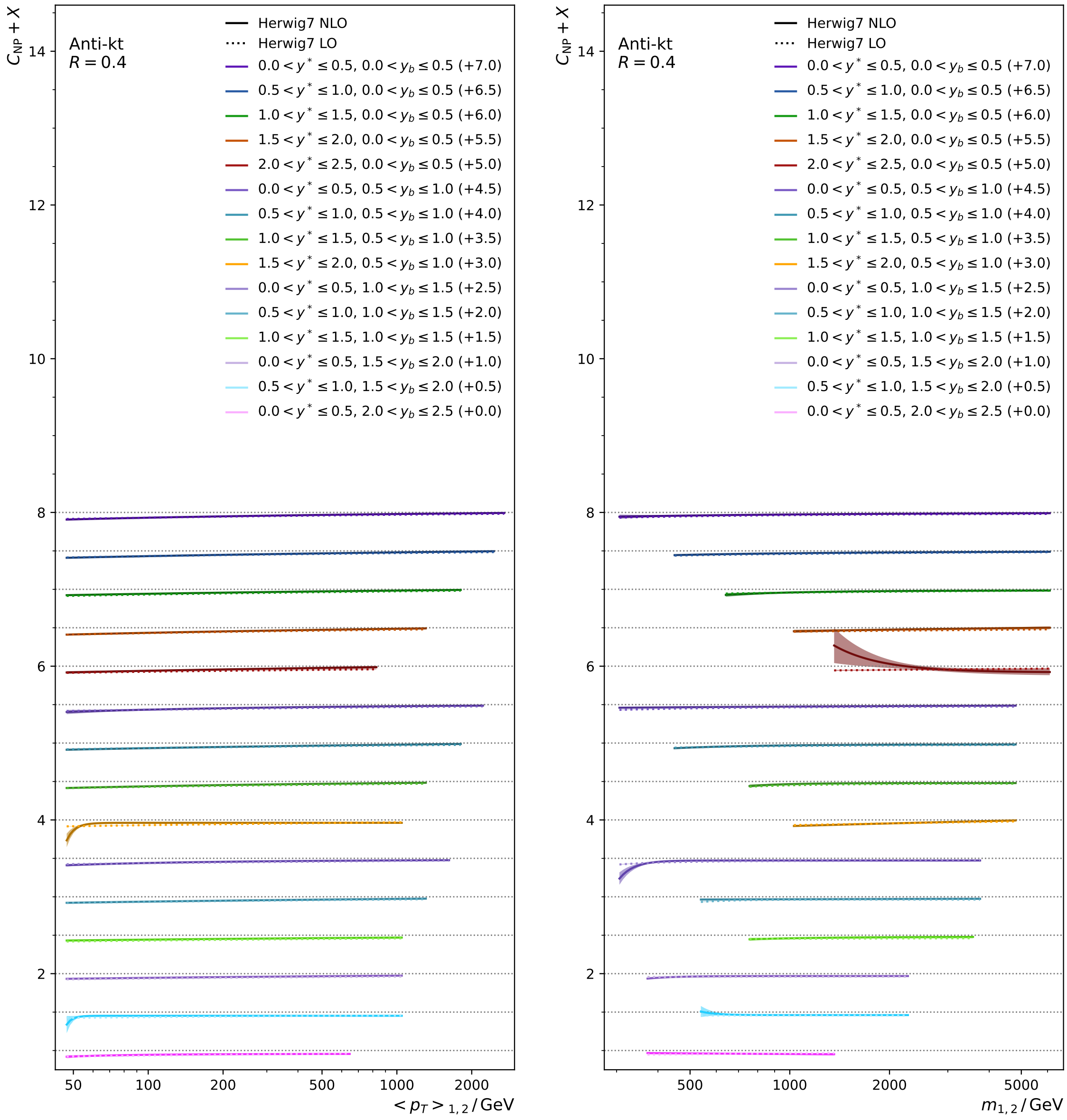

Figure 13: C_{NP} vs. dijet $\langle p_{\mathrm{T}}\rangle_{1,2}$ (left) and mass $m_{1,2}$ (right) using LO (dotted) and NLO MEs (solid lines) in HERWIG7 predictions for anti-k_{T} jets with $R = 0.4$. The fitted curves are shown for all 15 defined phase space intervals in (y_{b}, y^*) with bands indicating the statistical uncertainty. The factors are shifted with respect to unity by constant offsets.

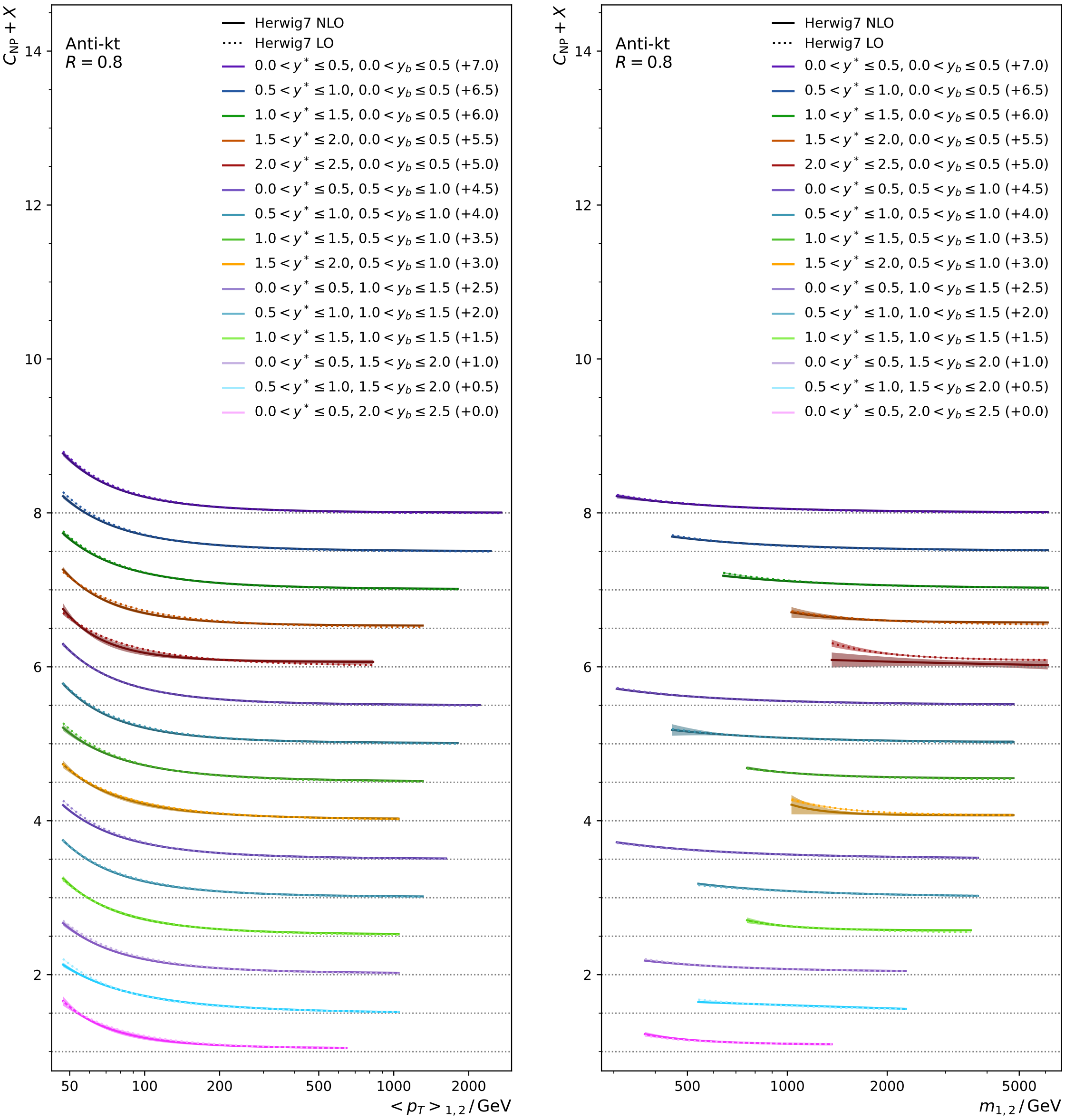

Figure 14: Same as Fig. 13 but for anti-k_T jets with $R = 0.8$.

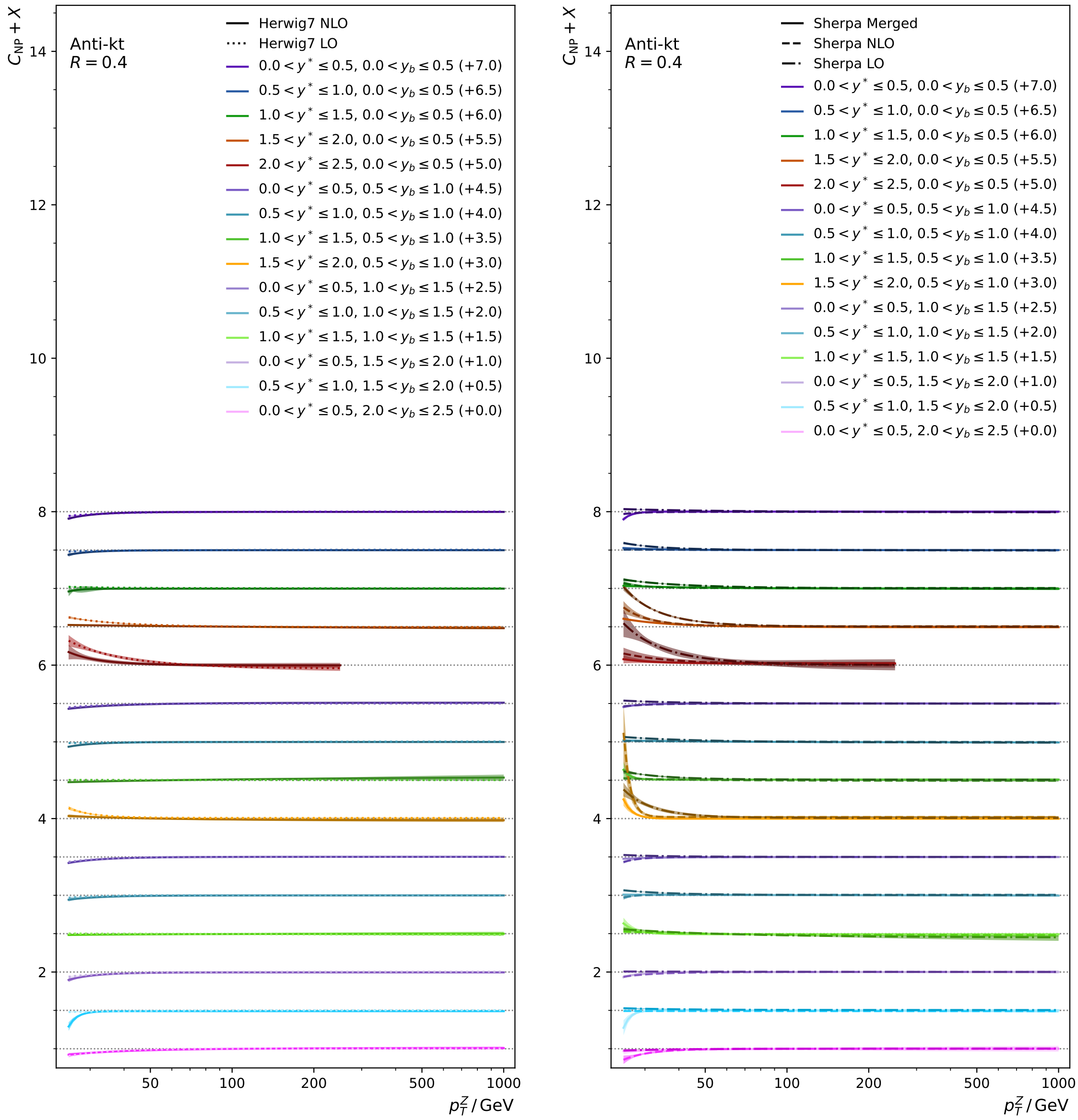

Figure 15: C_{NP} vs. $p_{\text{T,Z}}$ from HERWIG7 (left) using LO (dotted) and NLO MEs (solid lines), and from SHERPA (right) using LO (dash-dotted), NLO (dashed), and multileg-merged MEs (solid lines) for anti-k_{T} jets with $R = 0.4$. The fitted curves are shown for all 15 defined phase space intervals in (y_{b}, y^*) with bands indicating the statistical uncertainty. The factors are shifted with respect to unity by constant offsets.

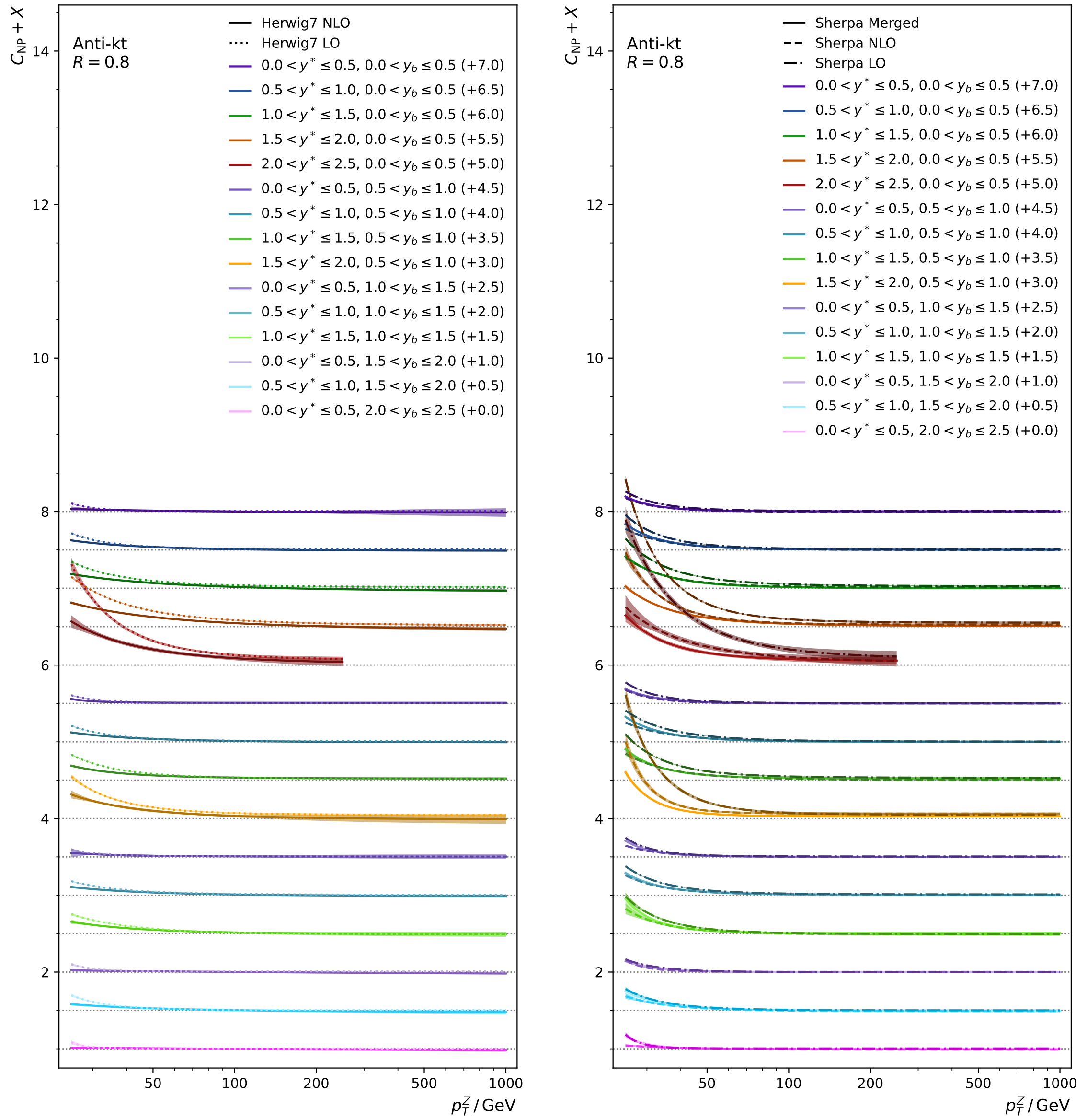

Figure 16: Same as Fig. 15 but for anti-k_T jets with $R = 0.8$.

References

[1] R. Boughezal, J. Campbell, R. K. Ellis, C. Focke, W. Giele, X. Liu and F. Petriello, *Z-boson production in association with a jet at next-to-next-to-leading order in perturbative QCD*, Phys. Rev. Lett. **116**, 152001 (2016), doi:10.1103/PhysRevLett.116.152001 [preprint doi:10.48550/arXiv.1512.01291].

[2] A. Gehrmann-De Ridder, T. Gehrmann, E. W. N. Glover, A. Huss and T. A. Morgan, *The NNLO QCD corrections to Z boson production at large transverse momentum*, J. High Energy Phys. **07**, 133 (2016), doi:10.1007/JHEP07(2016)133 [preprint doi:10.48550/arXiv.1605.04295].

[3] J. Currie, A. Gehrmann-De Ridder, T. Gehrmann, E. W. N. Glover, A. Huss and J. Pires, *Precise predictions for dijet production at the LHC*, Phys. Rev. Lett. **119**, 152001 (2017), doi:10.1103/PhysRevLett.119.152001 [preprint doi:10.48550/arXiv.1705.10271].

[4] M. Czakon, A. van Hameren, A. Mitov and R. Poncelet, *Single-jet inclusive rates with exact color at $\mathcal{O}(\alpha_s^4)$*, J. High Energy Phys. **10**, 262 (2019), doi:10.1007/JHEP10(2019)262 [preprint doi:10.48550/arXiv.1907.12911].

[5] X. Chen, T. Gehrmann, E. W. N. Glover, A. Huss and J. Mo, *NNLO QCD corrections in full colour for jet production observables at the LHC*, J. High Energy Phys. **09**, 025 (2022), doi:10.1007/JHEP09(2022)025 [preprint doi:10.48550/arXiv.2204.10173].

[6] H. Abramowicz et al., *Combination of measurements of inclusive deep inelastic $e^{\pm}p$ scattering cross sections and QCD analysis of HERA data*, Eur. Phys. J. C **75**, 580 (2015), doi:10.1140/epjc/s10052-015-3710-4 [preprint doi:10.48550/arXiv.1506.06042].

[7] A. Ablat, S. Dulat, T.-J. Hou, J. Huston, P. Nadolsky, I. Sitiwaldi, K. Xie and C. -P. Yuan, *Impact of LHC precision measurements of inclusive jet and dijet production on the CTEQ-TEA global PDF fit*, Phys. Rev. D **111**, 036033 (2025), doi:10.1103/PhysRevD.111.036033 [preprint doi:10.48550/arXiv.2412.00350].

[8] T.-J. Hou et al., *New CTEQ global analysis of quantum chromodynamics with high-precision data from the LHC*, Phys. Rev. D **103**, 014013 (2021), doi:10.1103/PhysRevD.103.014013 [preprint doi:10.48550/arXiv.1912.10053].

[9] R. D. Ball et al., *The path to proton structure at 1% accuracy*, Eur. Phys. J. C **82**, 428 (2022), doi:10.1140/epjc/s10052-022-10328-7 [preprint doi:10.48550/arXiv.2109.02653].

[10] T. Cridge, L. A. Harland-Lang and R. S. Thorne, *The impact of LHC jet and Z p_T data at up to approximate N^{3}LO order in the MSHT global PDF fit*, Eur. Phys. J. C **84**, 446 (2024), doi:10.1140/epjc/s10052-024-12771-0 [preprint doi:10.48550/arXiv.2312.12505].

[11] M. M. Horzela, *Measurement of triple-differential Z+jet cross sections with the CMS detector at 13 TeV and modelling of large-scale distributed computing systems*, PhD thesis, Karlsruher Institut für Technologie, Karlsruhe, Germany (2023), doi:10.5445/IR/1000165566.

[12] CMS collaboration: A. M. Sirunyan et al., *Measurement of the triple-differential dijet cross section in proton-proton collisions at $\sqrt{s} = 8\,TeV$ and constraints on parton distribution functions*, Eur. Phys. J. C **77**, 746 (2017), doi:10.1140/epjc/s10052-017-5286-7 [preprint doi:10.48550/arXiv.1705.02628].

[13] CMS collaboration: A. Hayrapetyan et al., *Measurement of multidifferential cross sections for dijet production in proton–proton collisions at $\sqrt{s} = 13\,TeV$*, Eur. Phys. J. C **85**, 72 (2025), doi:10.1140/epjc/s10052-024-13606-8 [preprint doi:10.48550/arXiv.2312.16669].

[14] M. Cacciari, G. P. Salam and G. Soyez, *The anti-k_t jet clustering algorithm*, J. High Energy Phys. **04**, 063 (2008), doi:10.1088/1126-6708/2008/04/063 [preprint doi:10.48550/arXiv.0802.1189].

[15] ATLAS collaboration: G. Aad et al., *The ATLAS experiment at the CERN Large Hadron Collider*, J. Instrum. **3**, S08003 (2008), doi:10.1088/1748-0221/3/08/S08003.

[16] CMS collaboration: S. Chatrchyan et al., *The CMS experiment at the CERN LHC*, J. Instrum. **3**, S08004 (2008), doi:10.1088/1748-0221/3/08/S08004.

[17] Particle data group: R. L. Workman et al., *Review of particle physics*, Prog. Theor. Exp. Phys. 083C01 (2022), doi:10.1093/ptep/ptac097.

[18] T. Aaltonen et al., *Measurement of inclusive jet cross sections in $z/\gamma^*(\to e^+e^-)$ + jets production in $p\bar{p}$ collisions at $\sqrt{s} = 1.96$ TeV*, Phys. Rev. Lett. **100**, 102001 (2008), doi:10.1103/PhysRevLett.100.102001 [preprint doi:10.48550/arXiv.0711.3717].

[19] D0 collaboration: V. M. Abazov et al., *Measurement of the inclusive jet cross section in $p\bar{p}$ collisions at $\sqrt{s} = 1.96$ TeV*, Phys. Rev. D **85**, 052006 (2012), doi:10.1103/PhysRevD.85.052006 [preprint doi:10.48550/arXiv.1110.3771].

[20] CMS collaboration: V. Khachatryan et al., *Constraints on parton distribution functions and extraction of the strong coupling constant from the inclusive jet cross section in pp collisions at $\sqrt{s} = 7$ TeV*, Eur. Phys. J. C **75**, 288 (2015), doi:10.1140/epjc/s10052-015-3499-1 [preprint doi:10.48550/arXiv.1410.6765].

[21] ATLAS collaboration: G. Aad et al., *Measurement of inclusive dijet cross-sections in proton-proton collisions at $\sqrt{s} = 13$ TeV with the ATLAS detector*, (arXiv preprint) doi:10.48550/arXiv.2512.19073.

[22] M. Horzela and C. Verstege, *MCRun: Scalable MC event generation and Rivet analysis*, Zenodo (2024), doi:10.5281/zenodo.14530596.

[23] M. Rieger et al., *riga/law*, Zenodo (2024), doi:10.5281/zenodo.13952360.

[24] C. Bierlich et al., *Robust independent validation of experiment and theory: Rivet version 3*, SciPost Phys. **8**, 026 (2020), doi:10.21468/SciPostPhys.8.2.026 [preprint doi:10.48550/arXiv.1912.05451].

[25] M. Bähr et al., *Herwig++ physics and manual*, Eur. Phys. J. C **58**, 639 (2008), doi:10.1140/epjc/s10052-008-0798-9 [preprint doi:10.48550/arXiv.0803.0883].

[26] J. Bellm et al., *Herwig 7.0/Herwig++ 3.0 release note*, Eur. Phys. J. C **76**, 196 (2016), doi:10.1140/epjc/s10052-016-4018-8 [preprint doi:10.48550/arXiv.1512.01178].

[27] E. Bothmann et al., *Event generation with Sherpa 2.2*, SciPost Phys. **7**, 034 (2019), doi:10.21468/SciPostPhys.7.3.034 [preprint doi:10.48550/arXiv.1905.09127].

[28] M. Cacciari, G. P. Salam and G. Soyez, *FastJet user manual*, Eur. Phys. J. C **72**, 1896 (2012), doi:10.1140/epjc/s10052-012-1896-2 [preprint doi:10.48550/arXiv.1111.6097].

[29] G. Bewick et al., *Herwig 7.3 release note*, Eur. Phys. J. C **84**, 1053 (2024), doi:10.1140/epjc/s10052-024-13211-9 [preprint doi:10.48550/arXiv.2312.05175].

[30] S. Plätzer and S. Gieseke, *Dipole showers and automated NLO matching in Herwig++*, Eur. Phys. J. C **72**, 2187 (2012), doi:10.1140/epjc/s10052-012-2187-7 [preprint doi:10.48550/arXiv.1109.6256].

[31] T. Gleisberg, S. Höche, F. Krauss, M. Schönherr, S. Schumann, F. Siegert and J. Winter, *Event generation with SHERPA 1.1*, J. High Energy Phys. **02**, 007 (2009), doi:10.1088/1126-6708/2009/02/007 [preprint doi:10.48550/arXiv.0811.4622].

[32] S. Dooling, P. Gunnellini, F. Hautmann and H. Jung, *Longitudinal momentum shifts, showering, and nonperturbative corrections in matched next-to-leading-order shower event generators*, Phys. Rev. D **87**, 094009 (2013), doi:10.1103/PhysRevD.87.094009 [preprint doi:10.48550/arXiv.1212.6164].

[33] S. Gieseke, P. Kirchgaeßer, S. Plätzer and A. Siodmok, *Colour reconnection from soft gluon evolution*, J. High Energy Phys. **11**, 149 (2018), doi:10.1007/JHEP11(2018)149 [preprint doi:10.48550/arXiv.1808.06770].

[34] S. Plätzer, *Colour evolution and infrared physics*, J. High Energy Phys. **07**, 126 (2023), doi:10.1007/JHEP07(2023)126 [preprint doi:10.48550/arXiv.2204.06956].

[35] A. H. Hoang, O. L. Jin, S. Plätzer and D. Samitz, *Matching hadronization and perturbative evolution: The cluster model in light of infrared shower cutoff dependence*, J. High Energy Phys. **07**, 005 (2025), doi:10.1007/JHEP07(2025)005 [preprint doi:10.48550/arXiv.2404.09856].

[36] J. R. Christiansen and T. Sjöstrand, *Color reconnection at future e^+e^- colliders*, Eur. Phys. J. C **75**, 441 (2015), doi:10.1140/epjc/s10052-015-3674-4 [preprint doi:10.48550/arXiv.1506.09085].

[37] J. R. Christiansen and P. Z. Skands, *String formation beyond leading colour*, J. High Energy Phys. **08**, 003 (2015), doi:10.1007/JHEP08(2015)003 [preprint doi:10.48550/arXiv.1505.01681].

[38] S. Gieseke, C. Röhr and A. Siódmok, *Colour reconnections in Herwig++*, Eur. Phys. J. C **72**, 2225 (2012), doi:10.1140/epjc/s10052-012-2225-5 [preprint doi:10.48550/arXiv.1206.0041].

[39] T. Affolder et al., *Charged jet evolution and the underlying event in proton-antiproton collisions at 1.8 TeV*, Phys. Rev. D **65**, 092002 (2002), doi:10.1103/PhysRevD.65.092002.

[40] D. Acosta et al., *Underlying event in hard interactions at the Fermilab Tevatron $\bar{p}p$ collider*, Phys. Rev. D **70**, 072002 (2004), doi:10.1103/PhysRevD.70.072002 [preprint doi:10.48550/arXiv.hep-ex/0404004].

[41] T. Aaltonen et al., *Studying the underlying event in Drell-Yan and high transverse momentum jet production at the Tevatron*, Phys. Rev. D **82**, 034001 (2010), doi:10.1103/PhysRevD.82.034001 [preprint doi:10.48550/arXiv.1003.3146].

[42] CMS collaboration: S. Chatrchyan et al., *Measurement of the underlying event in the Drell–Yan process in proton–proton collisions at $\sqrt{s}$ = 7 TeV*, Eur. Phys. J. C **72**, 2080 (2012), doi:10.1140/epjc/s10052-012-2080-4 [preprint doi:10.48550/arXiv.1204.1411].

[43] ATLAS collaboration: G. Aad et al., *Measurement of distributions sensitive to the underlying event in inclusive Z-boson production in pp collisions at $\sqrt{s}$ = 7 TeV with the ATLAS detector*, Eur. Phys. J. C **74**, 3195 (2014), doi:10.1140/epjc/s10052-014-3195-6 [preprint doi:10.48550/arXiv.1409.3433].

[44] CMS collaboration: A. M. Sirunyan et al., *Measurement of the underlying event activity in inclusive Z boson production in proton-proton collisions at $\sqrt{s}$ = 13 TeV*, J. High Energy Phys. **07**, 032 (2018), doi:10.1007/JHEP07(2018)032 [preprint doi:10.48550/arXiv.1711.04299].

[45] ATLAS collaboration: G. Aad et al., *Measurement of distributions sensitive to the underlying event in inclusive Z boson production in pp collisions at $\sqrt{s}$ = 13 TeV with the ATLAS detector*, Eur. Phys. J. C **79**, 666 (2019), doi:10.1140/epjc/s10052-019-7162-0 [preprint doi:10.48550/arXiv.1905.09752].

[46] S. Frixione and B. R. Webber, *Matching NLO QCD computations and parton shower simulations*, J. High Energy Phys. **06**, 029 (2002), doi:10.1088/1126-6708/2002/06/029 [preprint doi:10.48550/arXiv.hep-ph/0204244].

[47] CMS collaboration: A. M. Sirunyan et al., *Development and validation of HERWIG 7 tunes from CMS underlying-event measurements*, Eur. Phys. J. C **81**, 312 (2021), doi:10.1140/epjc/s10052-021-08949-5 [preprint doi:10.48550/arXiv.2011.03422].

[48] S. Schumann and F. Krauss, *A parton shower algorithm based on Catani-Seymour dipole factorisation*, J. High Energy Phys. **03**, 038 (2008), doi:10.1088/1126-6708/2008/03/038 [preprint doi:10.48550/arXiv.0709.1027].

[49] S. Höche, F. Krauss, M. Schönherr and F. Siegert, *A critical appraisal of NLO+PS matching methods*, J. High Energy Phys. **09**, 049 (2012), doi:10.1007/JHEP09(2012)049 [preprint doi:10.48550/arXiv.1111.1220].

[50] S. Höche, F. Krauss, M. Schönherr and F. Siegert, *QCD matrix elements + parton showers. The NLO case*, J. High Energy Phys. **04**, 027 (2013), doi:10.1007/JHEP04(2013)027 [preprint doi:10.48550/arXiv.1207.5030].

[51] T. Gehrmann, S. Höche, F. Krauss, M. Schönherr and F. Siegert, *NLO QCD matrix elements + parton showers in $e^+e^- \to$ hadrons*, J. High Energy Phys. **01**, 144 (2013), doi:10.1007/JHEP01(2013)144 [preprint doi:10.48550/arXiv.1207.5031].

[52] K. Hamilton and P. Nason, *Improving NLO-parton shower matched simulations with higher order matrix elements*, J. High Energy Phys. **06**, 039 (2010), doi:10.1007/JHEP06(2010)039 [preprint doi:10.48550/arXiv.1004.1764].

[53] S. Höche, F. Krauss, M. Schönherr and F. Siegert, *NLO matrix elements and truncated showers*, J. High Energy Phys. **08**, 123 (2011), doi:10.1007/JHEP08(2011)123 [preprint doi:10.48550/arXiv.1009.1127].